The Role of the Topological Constraints in the Chain Dynamics in All-Polymer Nanocomposites

Petra Bačová,[†] Federica Lo Verso,[‡] Arantxa Arbe,[†] Juan Colmenero,[¶,†,‡] José A. Pomposo,[§,†,¶] and Angel J. Moreno[*,†,‡]

Centro de Física de Materiales (CSIC, UPV/EHU) and Materials Physics Center MPC, Paseo Manuel de Lardizabal 5, E-20018 San Sebastián, Spain, Donostia International Physics Center (DIPC), Paseo Manuel de Lardizabal 4, E-20018 San Sebastián, Spain, Departamento de Física de Materiales (UPV/EHU), Apartado 1072, E-20080 San Sebastián, Spain, and IKERBASQUE - Basque Foundation for Science, María Díaz de Haro, E-48013 Bilbao, Spain

E-mail: angeljose.moreno@ehu.eus

[*]To whom correspondence should be addressed

[†]Centro de Física de Materiales (CSIC, UPV/EHU) and Materials Physics Center MPC, Paseo Manuel de Lardizabal 5, E-20018 San Sebastián, Spain

[‡]Donostia International Physics Center (DIPC), Paseo Manuel de Lardizabal 4, E-20018 San Sebastián, Spain

[¶]Departamento de Física de Materiales (UPV/EHU), Apartado 1072, E-20080 San Sebastián, Spain

[§]IKERBASQUE - Basque Foundation for Science, María Díaz de Haro, E-48013 Bilbao, Spain

Abstract

We investigate all-polymer nanocomposites, formed by linear chains and single-chain polymer nanoparticles (SCNPs), by means of large-scale simulations. To distinguish the role of the soft penetrable character of the SCNPs in the topological constraints from other specific contributions present in experiments, the simulations for different compositions of the mixture are performed at constant density, and with identical segmental mobility and monomer excluded volume for the SCNPs and linear chains. Every composition leads to a well-dispersed nanocomposite with fully-penetrated nanofillers. Hence, unlike in the case of hard nanofillers, the SCNPs do not exert confinement effects on the linear chains, and only contribute to the topological constraints. We discuss the intramolecular dynamics of the linear chains in terms of the tube model. We determine the entanglement length of the linear chains by analysing their isoconfigurational mean paths (IMP) and the primitive paths (PP), as a function of the concentration and topology of the SCNPs. In the analysis we use different estimators proposed in the literature. The IMP and PP analysis in the nanocomposites with sparse SCNPs yields values of the entanglement length smaller and larger, respectively, than in the reference pure linear melt, though small variations are observed. A more consistent trend is found in the nanocomposites with globular SCNPs, where both the IMP and PP analysis unambiguously reveal that the linear chains are more entangled than in the pure linear melt. Such differences between the effects of SCNPs with different topologies are presumably related to the much higher fraction of threadable loops in the globular SCNPs, with respect to their sparse counterparts, which effectively lead to more topological constraints.

1 Introduction

Dispersion of nanoparticles (NP) in polymer matrices has turned out to be a very efficient way to design novel hybrid polymer-based materials.[1,2] Extensive experimental[3–6] and simulation[7–9] studies have shown that the level of actual improvement of the material properties is highly dependent of the polymer/nanofiller interactions. In the case of nanocomposites containing long, mutually entangled polymer chains, these interactions represent an additional factor in a complex description of the structure-related properties. The viscoelastic character of pure unfilled polymer melts is attributed to the topological constraints (called entanglements), which stem from the chain-chain interactions and their mutual uncrossability.[10] A theoretical framework representing these constraints as an effective tube around each polymer chain has gained general acceptance.[11–13] After the isotropic Rouse regime, the chain segments experience the topological constraints, and their motion becomes highly anisotropic. The lateral motion is strongly restricted and the chains perform longitudinal Rouse motion followed by longitudinal diffusion along the tube (reptation). At late times the chain fully escapes from the tube and performs isotropic difussion. The tube theory has been extended and applied on branched architectures by implementing new relaxation mechanisms,[14] achieving impressive results even for commercial polymers with random branching.[15,16]

Hence, it is no wonder that the tube theory was invoked in the attempt to explain polymer behavior in hybrid nanocomposite systems. In nanocomposites with nonattractive interactions two types of constraints affecting polymer motion have been proposed: entanglements, characterized by the tube diameter d_{tube}, and geometrical confinement induced by the impenetrable nanoparticles, with a characteristic length scale d_{geo}. Schneider *et al.*[17] have proposed that the combination of both mechanisms results in the motion of the polymer chains in an effective or 'apparent' tube of diameter d_{app}. A simple ansatz relating all the former length scales has been suggested:[17]

$$d_{\mathrm{app}}^{-2}(\phi) = d_{\mathrm{tube}}^{-2}(\phi) + d_{\mathrm{geo}}^{-2}(\phi), \tag{1}$$

where ϕ is the nanoparticle volume fraction. Thus, depending on the actual volume fraction of the nanofillers, topological or geometrical confinement effects dominate the motion of the chains.

The tube diameter d_{tube} in the nanocomposite cannot be directly obtained from experiments. Its value relies on assuming the validity of Eq. (1) and on a correct estimation of the apparent tube diameter d_{app} and the geometrical confinement length scale d_{geo}. On the one hand, the value of d_{app} can be obtained, e.g., by analysing the dynamic structure factor in terms of the theoretical expression predicted by the tube theory for pure linear melts[17,18] (note however the possible drawbacks of this analysis in terms of the investigated molecular weight and wavevectors[19,20]). On the other hand, the value of d_{geo} can be calculated from a void distance distribution function, where the nanoparticles are approximated by perfectly dispersed hard spheres.[21] However, it is usually very difficult to fulfill experimentally the assumption of perfect nanoparticle dispersion. The case of silica nanoparticles is a well-know example of this problem. In order to achieve a homogeneous dispersion, favourable enthalpic interactions between the nanoparticles are necessary. Still, if the nanoparticle/polymer attraction is too strong, dynamical heterogeneities in the adsorbed polymer layer come into play. At high nanoparticle loadings this leads to a network-like structure, where the confined adsorbed chains form bridges between the nanoparticles.[3,22] One way to create a 'soft' interphase and to tune the interaction with the polymer matrix is by modifying the nanoparticle surface with grafted chains.[5,6,23,24] A few experimental studies have reported tube parameters for this type of nanocomposites, obtained either by applying tube theory to fit neutron spin-echo data[23] or by estimating characteristic times from linear rheology spectra.[24]

In a long-lasting effort to get a good compatibility between the nanoparticles and the polymer matrix, all-polymer nanocomposites have gained increasing attention over past years. In all-polymer nanocomposites the nanoparticles have no 'hard' components, but are fully polymer-based objects. Rapidly advancing techniques for polymer synthesis have opened the door to a huge variety of polymer nano-objects with complex architectures, ranging from single-chain nanoparticles[25–29] to soft dendritic (hyperbranched) structures.[30,31] Single-chain nanoparticles (SCNPs) are prepared from linear precursors with functionalized groups through purely intramolecular

crosslinking, and are attracting increasing interest of researchers due to their potential applications in nanomedicine, biosensing or catalysis among others.[32] The shape of the SCNPs is strongly dependent of the synthesis protocol.[33] In general, synthesis in good solvent conditions lead to sparse SCNPs.[34,35] This is a direct consequence of the self-avoiding conformations adopted by the precursors in good solvent, where long loops, at the origin of an efficient folding into globular SCNPs, are rarely formed.[35,36] Instead, bonding is mostly promoted over short contour distances, resulting in sparse SCNP conformations resembling those of intrinsically disordered proteins.[33,37] Several sophisticated routes, based on the solvent quality[38] or on the use of long cross-linkers,[39] have been recently introduced to synthesize globular SCNPs through promoting bonding over long contour distances (see Supporting Information).

When used as nanofillers, fully polymeric nanoparticles seem to affect the linear polymer matrix in a peculiar way. In 2003 Mackay *et al.*[40] sparked interest in all-polymer nanocomposites, by highlighting an exceptional reduction of viscosity of long poly(styrene) (PS) chains after addition of compact spherical PS nanofillers of half the size of the linear chains. This reduction was associated with confinement of the chain, determined by comparing the average interparticle distance d_{av}:

$$d_{\mathrm{av}} = D\left(\left[\frac{\phi_m}{\phi}\right]^{1/3} - 1\right) \tag{2}$$

to the dimensions of the matrix chains.[41] In Eq. (2) D represents the nanoparticle diameter and $\phi_m = 2/\pi$ the maximum volume fraction for random packing. For dendritic poly(ethylene) nanoparticles embedded in a PS matrix, a non-monotonic dependence of the viscosity on the nanoparticle concentration was found.[42] In contrast with results in Ref.,[40] a viscosity drop was produced at low nanoparticle loadings, i.e. below the theoretical confinement threshold. Factors as an alteration of the free volume or a reduction in the entanglement density were ruled out, indicating as a possible origin of the viscosity drop the acceleration of the polymer segmental relaxation close to the soft surface of the dendrimeric nanoparticles. This acceleration of the segmental relaxation was previously proposed in a simulation study of all-PS nanocomposites.[43] Recently, the tube model was applied to analyze neutron spin-echo data of all-polymer nanocomposites formed by poly(methyl

methacrylate) (PMMA)-based SCNPs and poly(ethylene oxide) (PEO)-linear chains.[44] A direct comparison was made with a blend of linear PMMA- and PEO-chains, with the same composition and molecular weights as in the nanocomposite. At long times after the Rouse regime the PEO-chains exhibited faster dynamics in the nanocomposite than in the blend, and an exceptional broadening of the apparent tube with respect to the melt of pure PEO. Two possible mechanisms at the origin of this observation were proposed: confinement effects and a high amount of SCNP surface in contact with the polymer matrix.[44] Similarly, it has been shown that the presence of fuzzy nanoparticles increase the diffusion rate of the linear chains,[45] while the actual value of the increase depends on the softness and the internal structure of nanoparticles.

In general, experiments suggest that the polymer/nanoparticle affinity as well as the soft character of the corresponding interface are at the origin of the unusual observed dynamic behavior. However, there may be undesired contributions that are difficult to be removed experimentally, and that may hinder the microscopic interpretation of the experimental results in the all-polymers nanocomposites, as e.g., impurities, polydispersity or differences in density and segmental mobility with respect to the pure linear melt.

These undesired contributions can be removed in simulations, which therefore provide a valuable tool for getting insight into the fundamental mechanisms behind chain motion in all-polymer nanocomposites. With these ideas in mind, in this article we present extensive simulations of a simple bead-spring model of all-polymer nanocomposites consisting of globular SCNPs and linear chains and compare them with results of the pure melt of linear chains. The beads of the SCNPs and the linear chains are identical and the simulations are performed at fixed density. The chains are undistorted and their segmental dynamics are unaffected with respect to the linear melt. Therefore, the differences in the dynamics of the linear chains in the melt and in the nanocomposite originate exclusively from the soft, penetrable character of the SCNPs. We investigate several compositions of the nanocomposite. Moreover, we address the role of the particular nanoparticle shape in the topological constraints, by comparing the former results with an analogous nanocomposite with sparse SCNPs.

Following an approach similar to the one used in previous computational investigations in nanocomposites with impenetrable spheres representing hard nanoparticles,[18,46–49] we have determined the entanglement length in our all-polymer nanocomposites by analysing the primitive path (PP) of the polymer chains. The PP is identified as the shortest path between the end monomers of the chain that is compatible with the topological constraints.[50–53] As discussed in several works,[46,47] it is not clear whether, in the case of nanocomposites with impenetrable hard nanoparticles, these should be removed from the system before the computation of the PP ("phantom particle" approach[18,54]) or should be kept in the system, thus acting as additional obstacles ("frozen particle" approach[18,54]). As will be shown, this distinction is not necessary in our work, since SCNPs do not induce confinement: they are fully penetrated by the linear chains and contribute to the topological constraints. Moreover, we have performed an alternative analysis based on the isoconfigurational mean path (IMP) approach,[55] which obtains the tube path by averaging out fast fluctuations while keeping the uncrossability of the chains.

The analysis of both the IMP and PP unambiguously reveals that the presence of globular nanoparticles leads to a smaller entanglement length with respect to the pure linear melt, acting thus as additional topological constraints in the system. Still, the variations are moderate, with a maximum reduction of 30 % in the entanglement length at the highest investigated nanoparticle concentration of 60 %. In the case of the nanocomposites containing sparse nanofillers, the original entanglement length is essentially unaffected (IMP analysis) or increased (PP analysis), though small variations are found with respect to the pure linear melt. Such differences between the effects of SCNPs with different topologies are presumably related to the much higher fraction of threadable loops in the globular SCNPs, with respect to their sparse counterparts, which effectively lead to more topological constraints.

In general, the results reported in this article suggest that the topology and the soft and penetrable character of fully polymeric nanoparticles play a moderate role in the dynamical properties of all-polymer nanocomposites. Additional effects (polymer/nanoparticle interactions, changes in density or segmental relaxation, etc) may have a similar or stronger contribution to the measured

properties.

The article is organized as follows. In Section 2 we give model and simulation details. Static and dynamic properties are presented and discussed in Sections 3 and 4, respectively. In Section 5 we present a detailed analysis of the IMP and PP in the investigated all-polymer nanocomposites. In Section 6 we discuss the consequences of the applied analysis for the interpretation of dynamic results in terms of the tube model. Conclusions are given in Section 7.

2 Model and Simulation Details

We investigated six all-polymer nanocomposites containing globular SCNPs. In what follows these systems will be denoted as gNC1-6 according to the volume fraction of the SCNPs (see Table 1). We also investigated one nanocomposite with sparse SCNPs (system sNC). All the systems were simulated by using the Kremer-Grest bead-spring model,[56] where the monomeric units in both the SCNPs and the linear chains were represented by beads of diameter σ, and the elastic bonds between them were modelled by the finite-extension nonlinear elastic (FENE) potential:

$$U_{\mathrm{F}} = -\frac{1}{2} K_{\mathrm{F}} R_{\mathrm{F}}^2 \ln\left[1 - \left(\frac{r}{R_{\mathrm{F}}}\right)^2\right]. \tag{3}$$

A spring constant $K_{\mathrm{F}} = 30\varepsilon/\sigma^2$ and maximum bond length $R_{\mathrm{F}} = 1.5\sigma$ were used in order to assure small fluctuations around the average bond length ($l_0 = 0.97\sigma$) and guarantee the non-crossability of the chain segments. In what follows quantities will be expressed in simulation units: length unit σ, time unit $\tau_0 = (m_0\sigma^2/\varepsilon)^{1/2}$ and temperature unit $\varepsilon/k_{\mathrm{B}}$, with m_0 the bead mass and k_{B} the Boltzmann constant. The non-bonded interaction between any two beads at a mutual distance r was represented by a Lennard-Jones (LJ) potential:

$$U_{\mathrm{LJ}}(r) = \begin{cases} 4\varepsilon\left[\left(\frac{\sigma}{r}\right)^{12} - \left(\frac{\sigma}{r}\right)^{6}\right] + U_{\mathrm{shift}} & \text{for } r \le r_{\mathrm{c}}, \\ 0 & \text{for } r > r_{\mathrm{c}}. \end{cases} \tag{4}$$

In all the investigated systems a purely repulsive LJ potential was applied for the self-interactions, i.e., for polymer/polymer and NP/NP interactions, with $\varepsilon = k_{\mathrm{B}}T$, a cutoff distance $r_{\mathrm{c}} = 2^{1/6}\sigma$ and a shifting factor $U_{\mathrm{shift}} = k_{\mathrm{B}}T$. We used the same parameters for the cross-interaction (NP/polymer) in the system with sparse nanoparticles, which showed perfect NP/polymer mixing. However, in the systems with globular nanoparticles, using identical nonattractive self- and cross-interactions led to phase separation of the linear chains and the nanoparticles. Therefore, in the systems gNC1-6 we kept the former repulsive LJ potential for the self-interactions, and used a slightly attractive LJ potential for the NP/polymer interaction, with parameters $r_{\mathrm{c}} = 2.5\sigma$, $\varepsilon = 0.5k_{\mathrm{B}}T$ and $U_{\mathrm{shift}} = 0$. This was sufficient to achieve perfect mixing of the linear chains and the globular nanoparticles without altering the average conformations of the linear chains, which were essentially undistorted with respect to the pure linear melt (see below).

In addition to the above mentioned potentials, an intramolecular bending potential,

$$U_{\mathrm{bend}}(\theta) = C_2\theta^2 + C_4\theta^4, \tag{5}$$

was applied to the linear chains in all the investigated systems, with θ the angle between consecutive bond vectors. We used the parameters $C_2 = 0.92504230$ and $C_4 = -0.054183683$, which in practice resulted in a potential undistinguishable from the cosine potential used in Ref.[57] (differences between both potentials only arise at very large angles that are never accessed due to excluded volume repulsion). Therefore the properties of the pure linear melt are identical to those already reported for the system of Ref.,[57] which was investigated at the same density and with the same LJ and FENE interactions as those used here. Thus, the bending potential with the former parameters C_2, C_4 provides a moderate semiflexible character to the chains, with a characteristic ratio[57] $C_\infty \approx 3.4$. The corresponding entanglement length for this model is $N_{\mathrm{e}} \approx 25$ according to the PP analysis of Ref.[50] Thus, the semiflexible character produces a decrease of the entanglement length with respect to the fully-flexible case ($N_{\mathrm{e}} \approx 65$ or ≈ 85 according to the different PP constructions of Refs.[50] and[58] , respectively). This allows to simulate more strongly entangled

systems than by using fully-flexible counterparts of the same molecular weight.

As aforementioned, we investigate the role of the nanoparticle architecture (sparse or globular) in the topological constraints experienced by the linear chains. To enhance differences between both types of nanoparticles, we also applied the bending potential of Eq. (5) to the sparse nanoparticles, in order to achieve more open NP conformations and to increase the number of NP/polymer contacts. On the contrary, no bending was applied to the globular nanoparticles, in order to achieve NP conformations as compact as possible.

The globular and sparse nanoparticles were generated by the methods reported in Refs.[38] and[35] , respectively (see also Supporting Information). The nanocomposite was obtained as follows. First, the nanoparticles were randomly placed in the simulation box at a dilute concentration, preventing intermolecular concatenations. Then the linear chains were grown in the simulation box, rejecting insertions resulting in overlaps ($r < 0.85\sigma$) with previously inserted beads. Once the full system was constructed, it was slowly compressed and equilibrated in sucessive steps up to the target melt density. The melt of pure linear chains was also generated as the reference system.

In all systems the investigated density was fixed to $\rho = 0.85\sigma^{-3}$, which corresponds to melt conditions,[56] and the length of the linear chains was fixed to $N = 200$ beads. In the pure linear system this corresponds to $Z = N/N_e \approx 8$ entanglements per chain.[57] The compositions of the different investigated nanocomposites ranged from 10 % to 60 % in the weight fraction of nanoparticle beads. Since all the beads in the system have the same size and mass, the volume fraction ϕ is identical to the weight fraction. Further details on the compositions of the investigated systems are given in Table 1. The simulations were performed with the GROMACS package[59] at constant volume V, and temperature $\langle T \rangle = \varepsilon/k_B$. The Langevin thermostat was applied, with a friction constant $\Gamma = 0.5m_0/\tau_0$. A time step $\delta t = 0.003\tau_0$ was used for both the equilibration and production runs. The duration of the runs was of the order of 10^9 steps.

Table 1: Characteristics of the simulated systems: N_p and N_c stand for the number of nanoparticles and linear chains in the system, respectively. M_p and M_c denote the number of beads per nanoparticle and per linear chain, respectively. Volume fractions refer to the NPs.

system	volume fraction ϕ	N_p	M_p	N_c	M_c
gNC1	0.1	14	520	316	200
gNC2	0.2	27	520	282	200
gNC3	0.3	41	520	245	200
gNC4	0.4	54	520	212	200
gNC5	0.5	68	520	175	200
gNC6	0.6	81	520	141	200
sNC	0.25	88	200	352	200
linear	—			352	200

3 Static properties

Figure 1 displays the average radius of gyration, $\langle R_g^2 \rangle^{1/2}$, of the linear chains and the nanoparticles in all the investigated systems (data are represented vs. the volume fraction of the nanoparticles). There is some stretching of the linear chains by increasing the concentration of the nanoparticles. This is not surprising due to the concomitant increase of energetic favorable contacts. Still, stretching is rather weak (less than 6 %) and just reflects a slight increase of the effective local stiffness. The conformations of the chains indeed remain Gaussian. This is demonstrated by comparing the results for $\langle R_g^2 \rangle^{1/2}$ and $\langle R_e^2/6 \rangle^{1/2}$ (with R_e the end-to-end radius), which are identical for ideal Gaussian chains.[10,60] No differences are found within error bars. The inverse effect is observed for the globular nanoparticles. By increasing their concentration they are exposed to more nonattractive self-interactions, and shrink up to 20 %. In all the systems the average radius of gyration of the linear chains is of the order of twice the nanoparticle radius.

The nanoparticles are cross-linked objects with permanent bonds, and therefore contain permanent loops in their internal structure. Figure 2 shows, for different investigated nanocomposites, the average size of the loop as a function of the number of beads in the loop. The observed trend is analogous to that of Figure 1, and, in average, the loops shrink by increasing the concentration of the nanoparticles. As can be seen in Figure 2, the globular architecture contains loops of the same size as the NP radius of gyration. Instead, in the sparse architecture the largest loop is clearly

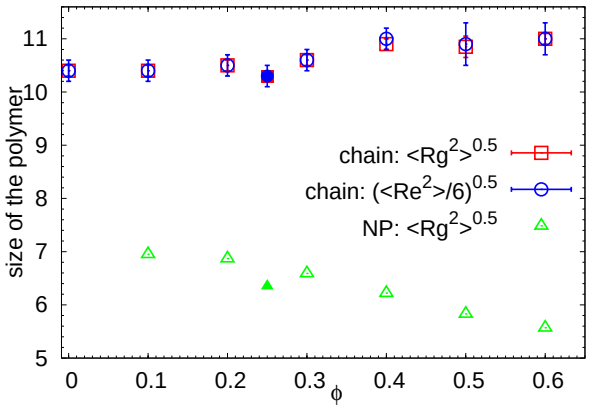

Figure 1: Average radius of gyration, $\langle R_g^2 \rangle^{1/2}$, for the linear chains (squares) and the nanoparticles (triangles) in all the investigated systems. Data are represented vs. the volume fraction ϕ of NPs ($\phi = 0$ for the pure linear melt). We include data (circles) of $\langle R_e^2/6 \rangle^{1/2}$ for the linear chains, with R_e the end-to-end radius. Within error bars these are identical to the corresponding data for $\langle R_g^2 \rangle^{1/2}$, demonstrating the Gaussianity of the linear chains in all the systems. Empty and filled symbols for $\phi > 0$ correspond to systems with globular and sparse NPs, respectively. Error bars for the NPs are smaller than the symbol size.

smaller than the NP size. This is a consequence of the different employed synthesis routes, where the formation of long loops is promoted (globular NPs)[38] or disfavored (sparse NPs).[35]

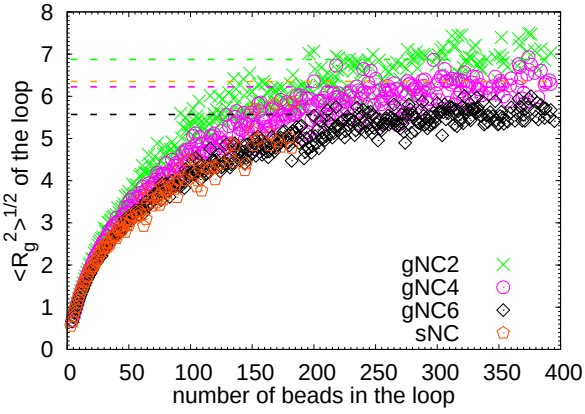

Figure 2: Radius of gyration of the permament loops in the globular nanoparticles (systems gNC2, gNC4 and gNC6) and in the sparse nanoparticles (system sNC). Data are represented vs. the number of beads in the corresponding loops. For comparison we include (dashed lines) the mean radius of gyration of the whole nanoparticle in the former systems.

Figure 3 shows the form factor $w(q)$ for the linear chains and the globular and sparse nanoparticles in three representative systems. In the fractal regime $1/R_g \ll q \ll 1/l_0$ the data can be

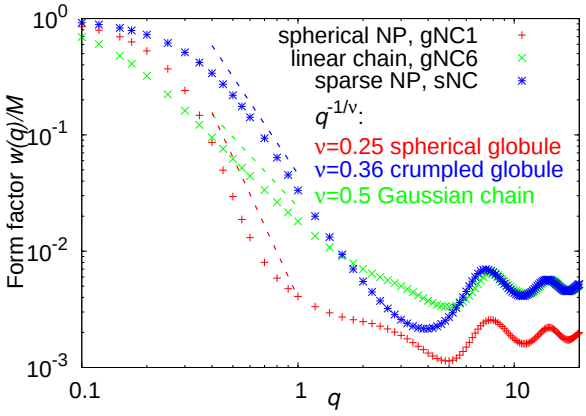

Figure 3: Form factor $w(q)$ normalized by the corresponding number of monomers M (M_p or M_c) of three selected components of the simulated systems: globular nanoparticles in gNC1 (red symbols), linear chains in gNC6 (green symbols) and sparse nanoparticles in sNC (blue symbols). The dashed lines describe scaling behavior $w(q) \sim q^{-1/\nu}$, with the exponent ν expected for Gaussian chains ($\nu = 0.5$), crumpled globules ($\nu = 0.36$), and for Porod scattering from compact spheres ($\nu = 0.25$). The latter are compared with the data for the linear chains, sparse NPs and globular NPs, respectively.

described by the power law[60] $w(q) \sim q^{-1/\nu}$. The obtained scaling exponents for each type of macromolecule are consistent with those expected for several archetype conformations: i) Gaussian chains ($\nu = 0.5$) in the case of the linear chains; ii) compact spheres in the case of the globular NPs, with the exponent $\nu = 1/4$ expected for Porod scattering;[60] iii) crumpled globules ($\nu \approx 0.36$) for the sparse nanoparticles, as anticipated in Refs.,[37,44] and resembling observations for ring polymers.[61] Analogous results are obtained for the three types of macromolecules in all the investigated systems.

As mentioned in the Introduction, the separation between topological entanglements and geometrical confinement, usually invoked in nanocomposites with hard NPs, may lose its meaning in all-polymer nanocomposites with soft deformable NPs. This idea is supported by Figure 4, which shows two typical snapshots for globular and sparse nanoparticles fully penetrated by surrounding linear chains. To confirm this point, we quantify in our system the degree of penetration of the nanoparticles by the linear chains. We consider that a nanoparticle is fully penetrated by a linear chain if some of the monomers of the chain is in the close vicinity of the center-of-mass of the nanoparticle. Figure 5 shows, for all the investigated systems, the partial radial distribution func-

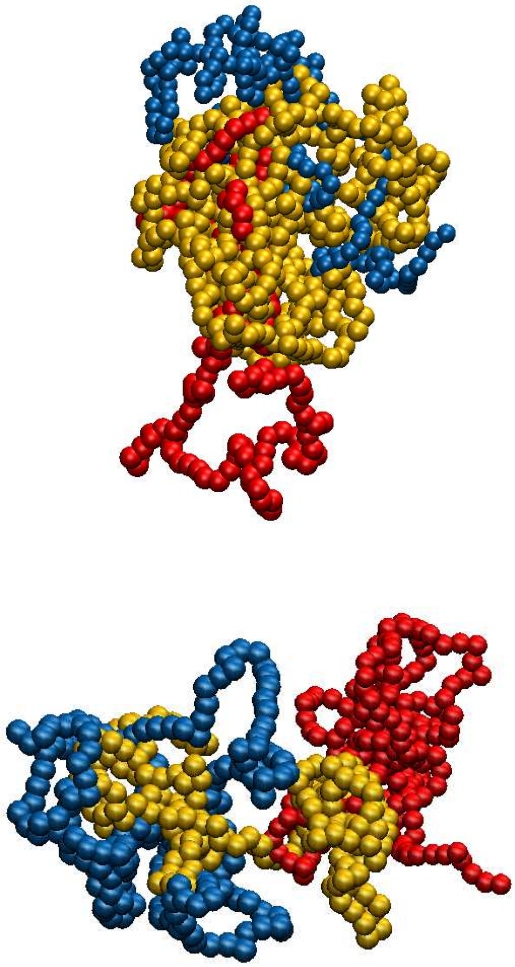

Figure 4: Top: Typical snapshot of a globular nanoparticle (yellow) in the gNC2 system, penetrated by two linear chains (blue and red). Bottom: Same as in the top panel, for a sparse nanoparticle in the sNC system.

tion $g(r)$ between the NP centers-of-mass and the monomers of the linear chains. The resulting $g(r)$'s are almost structureless, with just a weak correlation hole. Thus, $g(r=0) > 0.7$ for all the systems, and even $g(r=0) \lesssim 1$ for the largest concentrations of globular NPs. This demonstrates that the nanoparticles are fully penetrated by the linear chains, hence contributing to the topological constraints but not inducing confinement effects. A further test is given by calculating the number of 'contact monomers'. A monomer in a nanoparticle is defined as a contact monomer if it is at a distance $r < r_{\rm m}$ from at least one monomer of a polymer chain, where $r_{\rm m} = 1.5\sigma$ is the

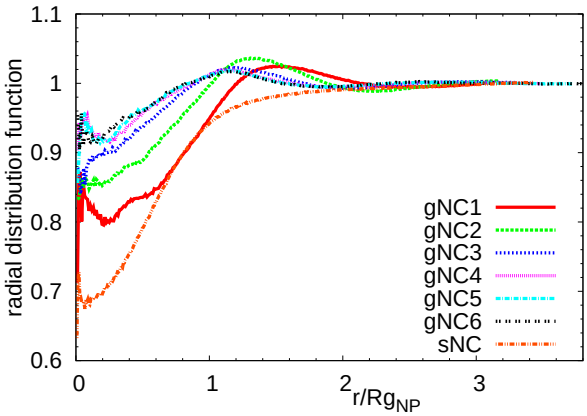

Figure 5: Radial distribution function of the monomers of the linear chains with respect to the centers-of-mass of the nanoparticles, for all the investigated nanoparticles. Distances are normalized by the respective radii of gyration of the NPs.

distance at the minimum of the all-monomer radial distribution function (not shown). We find that 97 % of the NP monomers are contact monomers in the sparse nanoparticles, and essentially 100 % in the globular nanoparticles at all the investigated concentrations.

In summary, the results presented in this section confirm that: i) the linear chains are essentially undistorted with respect to the pure linear melt; ii) the two types of employed nanoparticles, synthesized at high dilution, retain their sparse/globular character in the nanocomposites, and therefore provide, *a priori*, diferent topological constraints to their surrounding chains; iii) the nanoparticles are fully penetrated by the linear chains and do not induce geometric confinement on them.

4 Dynamic properties

Figure 6 shows the mean squared displacement (MSD, $\langle \Delta r^2(t) \rangle$) for the linear chains and the nanoparticles in some of the investigated nanocomposites. In the case of the linear chains the MSD is only computed for the middle monomers. Namely we take the 26 monomers in the center of the chain contour, i.e., the innermost entanglement segment. In this way the contributions of the faster outermost segments are eliminated, and the MSD provides a better representation of the dynamics of the linear chains inside the tube.

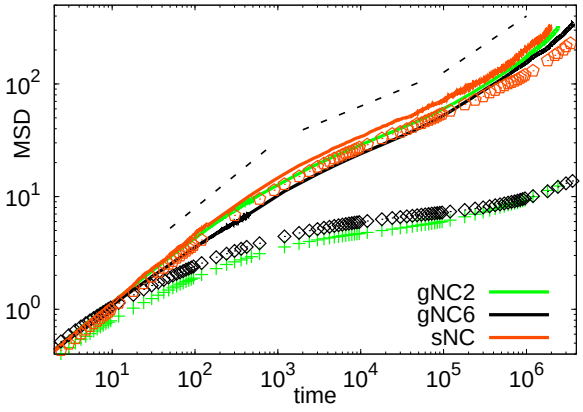

Figure 6: MSD for all monomers of the NPs (symbols), and for the middle monomers of the linear chains (solid lines). Data sets for the same system are depicted with identical colors (see legend). Dashed lines representing power law-behavior, $\langle \Delta r^2(t) \rangle \sim t^x$, are included for comparison. The exponents are, from short to long times, $x = 0.6, 0.3$ and 0.5.

First, it is worth noting that the simulated model leads, within statistics, to the same segmental relaxation of the linear chains in the different systems investigated, as revealed by the overlap of the corresponding data sets at short times. This is confirmed (see Figure 7) by computing the correlator, $\langle \mathbf{X}_p(t) \cdot \mathbf{X}_p(0) \rangle$, of the shortest Rouse mode, $\mathbf{X}_p = M_c^{-1} \sum_{j=1}^{M_c} \mathbf{r}_j(t) \cos[jp\pi/M_c]$ with $p = M_c - 1$, which probes the segmental relaxation.[10,60] All the correlators overlap within statistics. Therefore, dynamic differences in the simulated systems at later times arise only as a consequence of the different topological constraints induced by the respective concentrations and architectures of the nanoparticles.

In analogy with general observations in pure linear melts, after the short-time microscopic regime different sublinear regimes, $\langle \Delta r^2(t) \rangle \sim t^x$, are observed for the MSD of the linear chains, with exponents close to the ideal predictions from the tube theory. Thus, a first regime resembling Rouse-like dynamics ($x = 1/2$)[10,60] is found. The effective exponents slightly change, from $x = 0.6$ to $x = 0.5$, by increasing the concentration of globular nanoparticles. The exponent $x = 0.6$ observed at low ϕ is also found in the pure linear melt.[57] This deviation from ideal Rouse behavior may originate from non-Gaussian static correlations (not included in the Rouse model) at local scales, which are related to the semiflexible character introduced by the used bending potential.

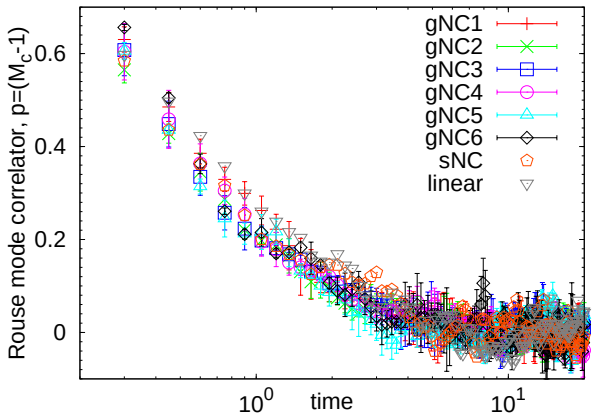

Figure 7: Time-dependence of the correlator of the shortest Rouse mode ($p = M_c - 1$) of the linear chains in the investigated systems.

The decrease to apparent ideal Rouse behavior, $x = 0.5$, at high ϕ likely arises from a compensation effect. The linear chains penetrate the globular nanoparticles, which are objects relaxing in a much slower fashion than the linear chains (see Figure 6). This breaks one of the basic assumptions of the Rouse model (fastly relaxing environment),[62] apparently decreasing the effective exponent in the MSD and compensating the increase associated to the local stiffness.

In all the systems, at the time scale of $t \sim 2000\tau_0$ that can be identified as the entanglement time τ_e, the monomers in the linear chains feel the uncrossability constraints and there is a deceleration in the MSD, leading to a second sublinear regime with an effective exponent $x \approx 0.3$. This is also the value found in the pure linear melt[57] and is slightly higher than the theoretical value $x = 1/4$ for the longitudinal Rouse dynamics inside the tube.[10,60] According to the tube theory, this 'Rouse-in-tube' regime ends at the Rouse time,[10,60] $\tau_R \approx \tau_e Z^2$, with Z the number of entanglements per chain. For the pure linear melt of this work[57] $Z \approx 8$ and $\tau_R \sim 10^5\tau_0$. In our nanocomposites, this time scale is of the same order of magnitude, though it seems to depend on the concentration and architecture of the NPs (see Figure 6). After the Rouse time, pure linear chains perform longitudinal diffusion along the tube (reptation), with a theoretical exponent $x = 1/2$, until the final transition to isotropic diffusion ($x = 1$) at the disengagement time[10,60] $\tau_d \approx 3Z\tau_R \sim 2 \times 10^6\tau_0$. Results in Figure 6 for the linear chains in the nanocomposites are apparently consistent with this expectation, yet an accurate estimation of the exponent is not possible due to the relatively short time window from τ_R to τ_d.

In summary, though they exhibit quantitative differences depending on the concentration and the architecture of the nanoparticles, the results in Figure 6 are apparently consistent with a tube-based picture for the dynamics of the linear chains in the investigated all-polymer nanocomposites.

Though the characterization of the dynamics of the nanoparticles is beyond the scope of this work, we comment some general features. First, as can be seen in Figure 6, the globular nanoparticles are much slower than the linear chains. At the time scales of the Rouse-in-tube regime for the linear chains, $2000 \lesssim t/\tau_0 \lesssim 10^5$, the MSD of the globular nanoparticles is severely slowed down and saturates to a plateau. This is a consequence of their compact and highly connected local structure, which impedes the broad fluctuations observed in the linear counterparts. At the onset of the reptation regime ($t \gtrsim 10^5$) for the linear chains, all the macromolecules start to mutually disentangle, and the MSD of the globular nanoparticles grows up again. The sparse nanoparticles, which are still slower than the linear chains, are much faster than their globular counterparts. Their sparse, less tightly linked, conformations allow for much broader fluctuations, and they do not show the intermediate plateau in the MSD.

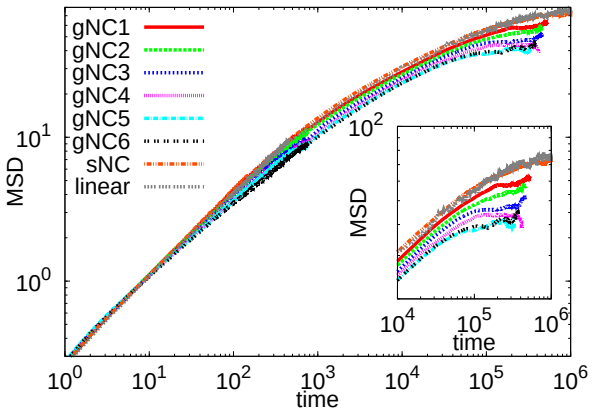

Figure 8: Mean squared displacement of the middle monomers of the linear chains in the simulations with fixed chain ends, for all the investigated systems. Inset: zoom of the plateaux that arise at $t \sim 10^5$.

To get a first characterization of the topological constraints experienced by the linear chains in the all-polymer nanocomposites, we have performed additional simulations with fixed chain ends, and analyzed the corresponding MSD. By fixing their end monomers, the longitudinal diffusion

of the linear chains is suppressed. To minimize the effect of the fixed chain ends on the monomer fluctuations, we compute again the MSD of the 26 middle monomers. The obtained results are shown in Figure 8. Due to the suppression of the longitudinal diffusion, the MSD reaches, at $t \sim \tau_R \sim 10^5$, an ultimate plateau that characterizes the fluctuations within the tube. A clear decrease of the plateau is observed by increasing the concentration of the globular nanoparticles. This suggests a stronger effect of the topological constraints induced by the globular nanoparticles on the linear chains. We quantify this effect in Section 5 by characterizing the tube path through two different approaches.

5 Isoconfigurational mean path and primitive path analysis

In this section we work with two approaches that use different procedures to characterize the tube from simulations: the isoconfigurational mean path (IMP) approach and the primitive path (PP) construction. The concept of IMP was introduced in Ref.,[55] and is based on the idea that the tube path associated to a given configuration of the macromolecule can be approximated by the coordinates of the monomers averaged over their isoconfigurational ensemble (IE). The latter is given by all the configurations at time $t = \tau_{iso}$, generated by starting at $t = 0$ from the same initial coordinates but with different velocities sampled from the Maxwell-Boltzmann (MB) distribution. If τ_{iso} is of the order of the entanglement time, the uncrossability of the chains is preserved, fast fluctuations within the tube are averaged out, and a smooth path is generated.

We ran simulations to generate the IE for a time scale $t = \tau_{iso} = 3000\tau_0 \approx 1.5\tau_e$. For the same initial configuration of the simulation box, we generated 50 trajectories by starting with different MB realizations of the velocities, and the 50 configurations obtained at $t = \tau_{iso}$ were used to get the averaged coordinates of the IMP of each chain. Finally, the static properties of each IMP (see below) were analyzed and averaged over all the chains. To improve statistics, the procedure was repeated for 10 different initial configurations of the box, equispaced by about 10^8 MD steps.

The PP approach constructs the tube paths by reducing all the chain countours between their re-

spective chain ends (which are kept fixed in space), with the condition of preserving the topological constraints (i.e., keeping the uncrossability of the chains). We followed the method proposed by Everaers *et al.*[50,51] Thus, we performed a simulation ('contraction run') where the end monomers of all the linear chains were fixed, at extremely low temperature $T = 0.001$, and where the bending potential and the *intramolecular* LJ interactions were switched off for all the macromolecules (both NPs and chains). All the intermolecular LJ interactions were kept, in order to allow for reduction of the chain/loop contour without violating the uncrossability condition. It must be noted that this procedure does not *minimize* the chain contour but the intramolecular energy. Strict minimization of the chain contour is achieved by geometric chain-shrinking methods,[52,53] through the use of geometric operations and supression of all the excluded volume without violating uncrossability. However, the implementation of geometric methods is extremely involved for the highly complex loopy architectures of the single-chain nanoparticles.

Following Ref.,[51] for the system of pure linear chains we used a time step $\delta t = 0.006\tau_0$ for the whole contraction run, with an initial value of the thermostat constant $\Gamma = 20\tau_0^{-1}$, which was changed to $\Gamma = 0.5\tau_0^{-1}$ after a few steps. In the nanocomposite systems we detected broader fluctuations of the bond lengths. Therefore we used a smaller time step $\delta t = 0.001\tau_0$, and moreover we decreased smoothly the value of Γ during the first 2×10^5 steps, from the initial $\Gamma = 20\tau_0^{-1}$ to the final value $\Gamma = 0.5\tau_0^{-1}$. Still, there were contraction runs where the length of some bonds exceeded the value of 1.3σ at some time (this was monitored on the fly). We excluded these runs from the further analysis, hence we discarded the PPs where a possible artificial bond crossing might have occurred during their generation.[51] To improve statistics, for each nanocomposite we used PP configurations obtained from typically 5-10 contraction runs. These runs were of the order of 10^6 steps. This time scale was much longer than the time needed for the contour length to decay to the ultimate plateau in its time dependence, corresponding to the equilibrium PP length. The CPU time for a single configuration in the IMP and PP runs was about 1 and 7 days, respectively, in a single AMD Opteron 6300.

Typical snapshots (system gNC3) of the IMP and PP of a globular nanoparticle and a penetrat-

ing linear chain are shown in Figure 9. At this point we would like to highlight some important facts. First of all, to the best of our knowledge, none of both procedures (IMP and PP) have been used before in nanocomposites with soft nanoparticles. The implementation of the IMP approach in these systems is straightforward and not fundamentally different from similar investigations in pure linear melts (just requiring simple averaging). However, in the case of the PP construction the handling of the nanoparticles may be tricky. Since the nanoparticles contain permanent loops, to generate their PPs we treated them in a similar way to polymer rings.[63] Thus, we did not fix in space any of the nanoparticle monomers and allowed them to relax freely during the contraction run. It has been shown that, as a consequence of this procedure, unthreaded polymer rings necessarily collapse into single points.[63] Unthreaded loops (i.e., loops not penetrated by linear chains) in our nanoparticles shrink under PP contraction but, in general, they do not collapse into single points. The reason is that, due to the cross-linked topology of the nanoparticles, threaded and unthreaded loops in the same nanoparticle form a mutually connected network, so that unthreaded loops cannot shrink independently of the threaded ones.

Recently, a dynamical analysis of the contacts between the mean paths has been reported for linear melts.[64] A similar analysis is however not suitable in our nanocomposites since they are systems fundamentally different from the case of the pure linear chains. In particular, the polymer chains in our nanocomposites have a tendency to align parallel to each other when they thread a group of close loops of the same nanoparticle. Under these conditions, the notion of the contact point between two mean paths is ill-defined, because there will be a whole sequence of beads within the critical distance used to define the mutual contact. Therefore, since we cannot track the individual contacts, we will use alternative ways of analysis based on the static properties of the tube path, represented by the IMP and the PP obtained from the simulations.

Starting with the assumption that both the IMP and PP are semiflexible objects, one can find a formula[50,51,65] for the normalized mean squared internal distances $\langle R^2(s)\rangle / s$:

$$\frac{\langle R^2(s)\rangle}{s} = l_b^2 \left[\frac{1+\langle\cos\theta\rangle}{1-\langle\cos\theta\rangle} - \frac{2\langle\cos\theta\rangle\left(1-\langle\cos\theta\rangle^s\right)}{s(1-\langle\cos\theta\rangle)^2} \right] \tag{6}$$

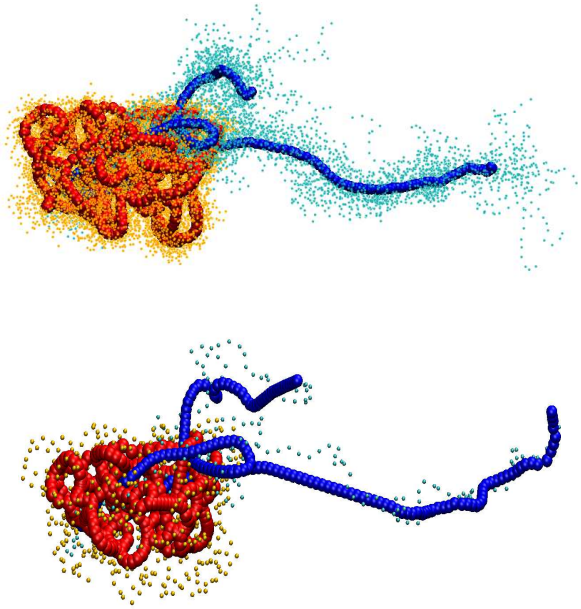

Figure 9: Typical snapshot (system gNC3) of the IMP and PP of a globular nanoparticle and a penetrating linear chain. The coordinates of the red (NP) and blue (chain) beads are obtained after applying the IMP procedure (top panel), and the PP construction (bottom panel). The coordinates of the real configurations used for such constructions are drawn as yellow (NP) and cyan dots (chain). For the sake of clarity, only 25 of the 50 configurations used for the IMP construction are displayed, and dots and beads in both panels are depicted smaller than the real monomer size.

where l_b is the bond length, θ is the angle between consecutive bonds, and $s = |i - j|$ is the chemical distance between two monomers i and j (monomers are labelled $i = 1, 2, \ldots, M_\mathrm{c}$ from one to the other chain end). Eq. (6) has been derived for the freely rotating chain (FRC) model.[50,51,65] In this model l_b and θ have constant values and no excluded volume is taken into account. Still, Eq. (6) has been shown to provide a good description of simulation data for real semiflexible chains,[65] as well as for primitive paths.[66] The quantity $\langle R^2(s)\rangle / s$ can be calculated directly from the coordinates of the tube path (IMP or PP), whereas l_b and $\langle \cos\theta \rangle$ can be also calculated as mean values from the IMP/PP data, or can be obtained as fit parameters. The average value of the cosine is related to the decay of the bond-bond correlation function of the tube path, assuming an

exponential decay:[60]

$$\frac{\left\langle \vec{b}_j \cdot \vec{b}_{j+s} \right\rangle}{l_\mathrm{b}^2} = \langle \cos\theta(s) \rangle = \langle \cos\theta \rangle^s = \exp(-l_\mathrm{b}/l_\mathrm{p}). \tag{7}$$

In Eq. (7) $\vec{b}_j$ is the bond vector connecting the positions of the monomers j and $j+1$ in the tube path, and l_p is the persistence length.[60] Since the tube path is a smooth object, the bond angles are small, and the FRC reduces to the worm-like chain (WLC) model. In the WLC $l_\mathrm{p} = l_\mathrm{k}/2$, where l_k is the Kuhn length.[60] By definition, N_e is the number of monomers per Kuhn segment of the tube path,[60] therefore:

$$N_\mathrm{e} = l_\mathrm{k}/l_\mathrm{b}. \tag{8}$$

Finally, by combining Eqs. (7) and (8), we get the first expression for determining the entanglement length:

$$N_\mathrm{e} = -\frac{2}{\ln(\langle \cos\theta \rangle)}. \tag{9}$$

Instead of analyzing the internal structure of the tube path, one can assume that at large scales the tube path has the form of a Gaussian coil. We will work with two N_e-estimators based on the relations (resulting from Gaussianity) between the end-to-end distance R_e and the contour length L of the tube path. The first one is the so-called 'classical S-coil estimator', which defines N_e as follows:[50]

$$N_\mathrm{e} = N_\mathrm{b} \frac{\left\langle R_\mathrm{e}^2 \right\rangle}{\langle L \rangle^2}, \tag{10}$$

where N_b stands for the number of bonds. The second one is the 'modified S-coil estimator':[58]

$$N_\mathrm{e} = N_\mathrm{b} \left(\frac{\left\langle L^2 \right\rangle}{\left\langle R_\mathrm{e}^2 \right\rangle} - 1 \right)^{-1}, \tag{11}$$

which operates with the second moment of the contour length, $\left\langle L^2 \right\rangle$, and in general overestimates the value of N_e for weakly entangled systems. It has been shown[46,58] that both S-coil estimators provide values of the entanglement length which are N_b-dependent, i.e., the obtained value of N_e

varies with the chain length. Nevertheless, the asymptotic, ideal infinite-chain limit is already reached for chains less entangled than those used in our model[46,58] ($Z \sim 8$). Hence, a reliable estimation of the ideal N_e is expected from our analysis.

In what follows we explore the three mentioned ways for calculating N_e (Eqs. (9) to (11)), paying particular attention to the correct estimation of the necessary parameters provided by the simulation data (l_b, $\langle \cos\theta \rangle$, $\langle R_e^2 \rangle$, $\langle L \rangle$ and $\langle L^2 \rangle$). Starting with Eq. (6), we looked closer at the bond length l_b between the monomers, by firstly checking its dependence on the position i along the tube path. It turns out that, whereas in the inner part of the tube path l_b is essentially independent of the position, as we approach the path ends the value of l_b changes. As a consequence of the higher mobility of the free chain ends, averaging in the IMP construction leads to a looser structure at the ends of the path than in the middle. On the contrary, fixing chain ends in the PP construction leads to a tauter structure at the path ends. Hence, the values of l_b in the IMP and PP are smaller and larger, respectively, than the values at the middle of the path (see Figure 10). These finite-size artifacts, originating from the distorsions at the path ends, affect the rest of the quantities involved in Eqs. (6) to (11) (e.g., the contour length through the relation $L = N_b l_b$). Therefore, to remove the end effects in our analysis, we used the former equations by omitting the 50 outermost monomers at each end of the tube path. Consequently, we used $N_b = N - 100$ in Eqs. (10) and (11).

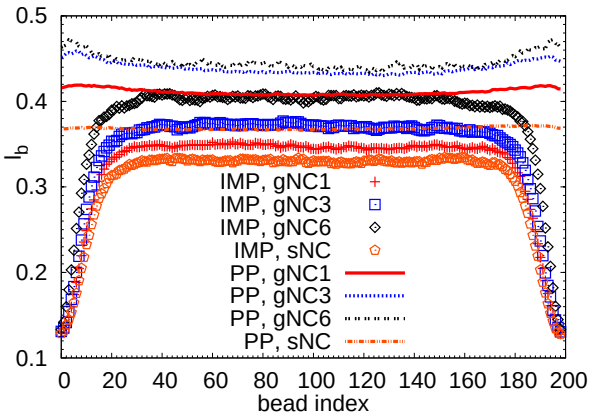

Figure 10: Bond length in the tube path vs. the position i of the monomer. Symbols and lines correspond to results for the IMP and PP, respectively.

Once the average value of l_b was determined from the tube path coordinates, we computed

$\left\langle R^2(s)\right\rangle/s$, inserted l_b in Eq. (6), and obtained $\langle\cos\theta\rangle$ as a fit parameter of $\left\langle R^2(s)\right\rangle/s$ to the right-hand-side of Eq. (6). Another option to estimate $\langle\cos\theta\rangle$ might be by fitting simulation data to Eq. (7). However, this is a less reliable procedure. Indeed, the bond-bond correlation functions of the tube paths have a complex shape and it is difficult to solve the purely exponential decay in particular ranges of s (see Ref.[66]). The data for $\left\langle R^2(s)\right\rangle/s$ together with the corresponding fits to Eq. (6) are presented in Figure 11. Eq. (6) provides a good description of the PPs. The agreement is worse for the IMPs, especially at moderate distances s. Finally, the values of $\langle\cos\theta\rangle$ collected from the former fits were inserted in Eq. (9), providing the first estimation of the entanglement length. The calculation of N_e based on the S-coil and modified S-coil (mS-coil) estimators (Eqs. (10) and (11)) was straightforward: we measured L and R_e by removing again the 50 outermost monomers at each end and inserted the measured values in Eqs. (10) and (11) to get the values of N_e.

In all cases the average values of N_e were obtained by using, for the simulation inputs in Eqs. (6) to (11), the corresponding values averaged over the generated tube paths (IMP or PP). On passing we mention that the values of $\langle L\rangle$ and $\langle L^2\rangle^{1/2}$ were $9-17\%$ larger in the PP than in the IMP. For the calculation of the error bars of N_e we differentiated Eqs. (6) to (11), and inserted the corresponding averages and standard deviations of the simulation inputs. The results for the entanglement length evaluated by the three employed methods (cosine, S-coil and mS-coil) are shown in Table 2, and displayed in Figure 12 as a function of the NP concentration. Regarding the reference pure linear melt, our model is very close to the model investigated in Ref.,[57] as mentioned in Section 2. A cosine-based analysis of the PP has been performed by Everaers *et al.* for the latter model,[50,51] yielding a value consistent with the one obtained in our work, $N_e \approx 23$.

We can make several conclusions from the information in Table 2 and Figure 12. First, the numerical values of the entanglement length N_e depend on both the representation of the tube path (IMP or PP) and the used estimator (cosine-based, S-coil or mS-coil). The dependence on the estimator is consistent with observations in Ref[46] for nanocomposites with hard NPs. The dependence on the tube representation was brought up in a study of a simple grid model,[67] and we

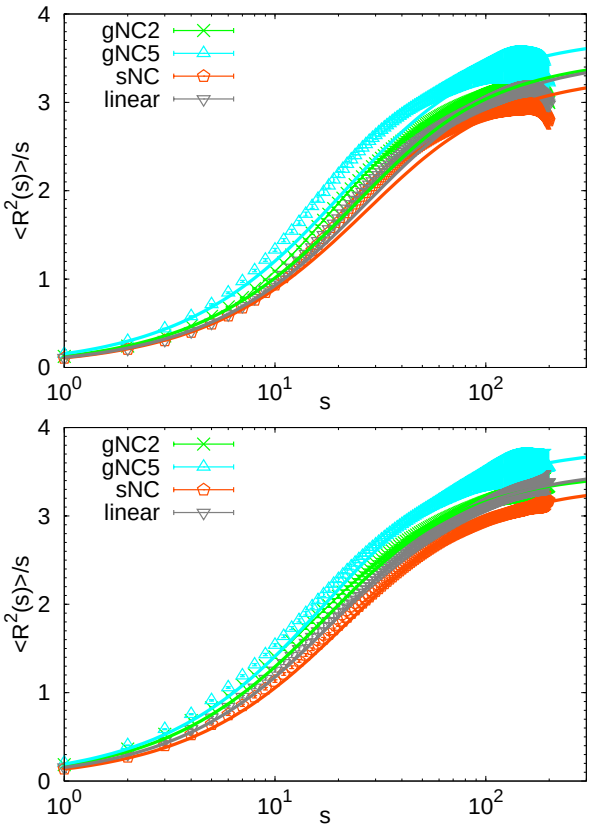

Figure 11: Normalized mean-squared internal distances, $R^2(s)/s$, for the IMPs (top) and PPs (bottom), represented vs. the contour distance s, for some selected systems. The simulation data are represented by symbols. The solid lines are fits to Eq. (6), with $\langle \cos\theta \rangle$ as the only fit parameter (see text).

will address this issue later on in the discussion. Having in mind these shortcomings, it is worthy of remark that the normalized entanglement length $N_e(\phi)/N_e(0)$, where $N_e(0)$ is the entanglement length for the pure linear melt, is almost independent of the estimator. As can be seen in Figure 12, for the same representation of the tube path (IMP or PP), the data sets of $N_e(\phi)/N_e(0)$ obtained by the different estimators show a very good agreement, especially in the case of the cosine-based and S-coil estimators.

The dependence of the results on the tube representation is mainly reflected in the sytem with sparse nanofillers. For the investigated concentration, the entanglement length obtained from the IMP analysis is slightly smaller than in the pure linear melt. The PP analysis yields a larger N_e in the nanocomposite, though differences with the pure linear melt are smaller than 8 %. A more

Table 2: Results for N_e in each of the investigated systems, obtained from the analysis of the IMP and PP. The results are given for the three used estimators (cosine-based, S-coil and mS-coil).

	isoconfigurational mean path			primitive path		
system	N_e(S-coil)	N_e(mS-coil)	$N_e(\cos\theta)$	N_e(S-coil)	N_e(mS-coil)	$N_e(\cos\theta)$
gNC1	24.8±0.9	32.1±0.3	28.3±0.6	18.4±0.8	22.1±0.2	20.8±0.5
gNC2	24.6±0.7	31.7±0.7	27.8±0.9	17.9±0.5	21.4±0.4	20.0±0.7
gNC3	23.2±0.4	29.5±0.1	26.1±0.8	17.0±0.4	20.2±0.1	19.1±0.6
gNC4	23.7±1.4	30.3±1.4	26.8±0.9	17.9±0.8	21.3±0.5	20.0±1.0
gNC5	22.2±1.3	28.0±1.6	24.2±1.4	18.2±1.1	21.8±1.2	19.7±1.1
gNC6	20.9±0.8	25.9±1.0	23.5±0.5	17.4±0.7	20.7±0.5	19.8±0.8
sNC	26.6±0.9	35.2±1.0	30.6±0.7	22.0±0.8	27.5±0.6	25.0±0.9
linear	27.2±1.0	36.4±1.0	31.0±0.8	20.6±0.6	25.6±0.4	23.2±0.5

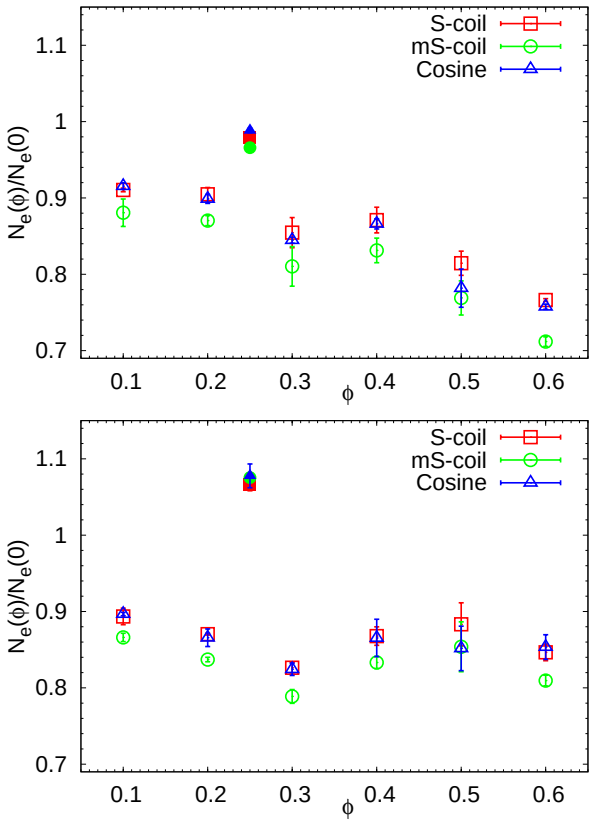

Figure 12: Results for N_e obtained from the analysis of the IMP and PP (top and bottom panels, respectively). The data are represented vs. the volume fraction ϕ of NPs ($\phi = 0$ for the pure linear melt), and are normalized by the respective values for the pure linear melt, $N_e(0)$. Empty and filled symbols correspond to systems with globular and sparse nanoparticles, respectively. Different colors correspond to the three estimators used to determine N_e (see legend).

consistent picture is found in the case of the nanocomposites filled with globular NPs. For both representations of the tube the values of N_e are smaller than in the linear melt for all the investigated concentrations of NPs. An inconspicuous evidence of non-montonic behavior in the concentration dependence of N_e can be detected, with an apparent minimum at $\phi \sim 0.3$ in both representations. The normalized entanglement lengths obtained from both representations of the tube show similar values up to $\phi \sim 0.4$. However, at higher concentrations the IMP analysis yields lower values than the PP analysis, resulting in a general decreasing trend of the entanglement length, down to about 25-30 % for the highest investigated ϕ. Instead, the PP analysis yields no systematic concentration dependence of N_e for $\phi > 0.1$.

6 Discussion

The key feature of our single-chain nanofillers is their soft, fully polymeric character. This feature gives rise to distinct structure-related properties of our all-polymer nanocomposites than those observed in systems with hard (e.g., silica-based) nanofillers. First of all, the linear chains can fully penetrate the SCNPs. In the case of globular SCNPs this means that the linear chains pass through a compact cross-linked loop-like structure. Such a deep insight into the internal arrangement of the nanocomposite is essential for the further explanation of the dynamical properties of the material, and in general it can not be obtained directly from experiments. Some all-polymer nanocomposites investigated in the literature share some structural similarities with our systems, as e.g. the presence of loops[45] and cross-links[40,41] in the architecture of the NPs. However, the lack of accurate information about the NP/polymer interphase region impedes us to make a critical comparison with our simulations.

Unlike it is usually found in experiments (e.g., due to different segmental mobilities of the NPs and the linear matrix[24,44]), the monomeric friction of the linear chains remains unaffected by the addition of the NPs. This feature facilitates the analysis of the translational motion of the linear chains in our nanocomposites. Negligible effects are found in the nanocomposite with sparse NPs.

However, the presence of globular NPs results in an evident deceleration of the linear chains at intermediate and long time scales. The deceleration is more pronounced in the system with high volume fraction of NPs. The quantification of this effect requires the application of a theoretical model, in this case the tube model. Having in mind the polymer-like nature of our nanofillers, the environment of the linear chains is closer to the mean-field tube idea of polymer melts with complex architectures rather than to the geometrically confined situation in hybrid solid/polymer nanocomposites. An usual strategy in simulation studies is to derive tube parameters from the analysis of the sublinear regimes in the MSD. This procedure however is affected by some implicit assumptions on the static properties of the tube, and has important shortcomings even in the simplest case of pure linear chains (see the recent discussion in Ref.[67]). Similar drawbacks are present in the estimation of the tube parameters from scattering functions,[20] and in particular if the chains are far from the limit of high molecular weight ($Z \sim 100$).[19,67] The analysis of dynamic observables as the MSD or the scattering function becomes even more problematic in our all-polymer nanocomposites, since they combine structural features as loops, chain ends, and cross-links acting as branch points. Indeed, these structures show dynamically different responses to topological constraints, and are treated in very different ways by the corresponding implementations of the tube model.[11,14,68]

Having in mind the limitations of the dynamics-based analysis, we have used an alternative procedure based on the characterization of the tube path, which has been represented by the IMP and the PP. The first encouraging step is that the analysis of the static properties of the tube path, both for the IMP and PP, provides the same qualitative trends as the model-independent results of the MSD. Still, the analysis yields quantitative results that depend on the used representation (IMP or PP) of the tube path, even by using the same estimator of N_e. These differences may be attributed to the different local structure of both semiflexible objects. In particular, the semiflexible character of the mean path is determined by the way the short time fluctuations are averaged out,[55,64] making the isoconfigurational average approach the most computationally demanding, but also the one that fully preserves the topology of the system.[64] On the other hand, while considering the primitive

path analysis of the nanocomposites, the collapse of the unthreaded nanoparticle loops affects the local arrangement of the system by creating 'free volume'. If we considered an extreme case where the whole nanoparticle fully collapsed into a single point, this situation would be similar to the 'phantom' approach in nanocomposites with hard NPs (where the NPs are removed from the simulation box before PP contraction). It has been shown that the analysis of the PP under the phantom approach yields larger values of N_e (i.e., a weaker degree of entanglement) than under the 'frozen' approach (PP contraction under full NP excluded volume).[46] A quantitative determination of the degree of threading/unthreading of the NP loops is very elaborated (see e.g., Ref.[69] for the case of ring polymers) and is beyond the scope of this work. Still, we speculate that the collapse of a significant fraction of unthreaded loops during the PP contraction may smoothen the dependence of N_e on the volume fraction, with respect to the much more pronounced trend revealed by the IMP analysis (Figure 12).

We also speculate that the different effect of the NP topology (sparse or globular) on the entanglement length of the linear chains is connected with the different degree of threading of the NP loops. Figure 13 shows the normalized distributions of loop sizes for the sparse and the globular NPs, where the loop size is defined as the number of beads in the loop. As a direct consequence of the different protocols used for their synthesis,[35,38] long loops are much more frequent in the globular NPs. Moreover, the sparse NPs contain a high fraction of small unthreadable loops. Namely, the loops with $n \leq 6$ beads represent a fraction of 60 % in the sparse NPs whereas the fraction is only 8 % in the globular ones. Such a large fraction of unthreadable loops is ineffective for constraining the linear chains, and moreover adds some effective stiffness to the NP contour, which tends to decrease the number of intermolecular contacts. Consequently, the entanglement length of the pure linear melt is essentially unaffected or increased under the presence of sparse NPs.

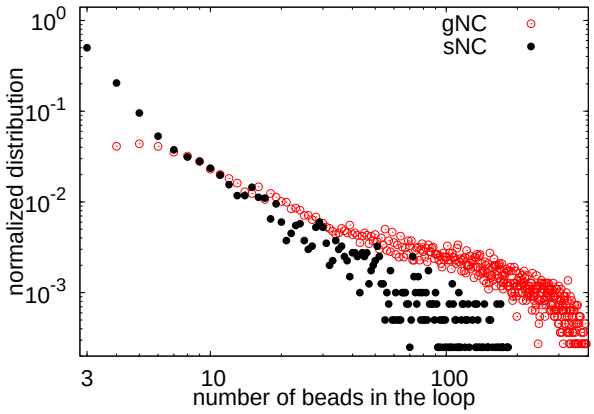

Figure 13: Normalized distribution of the loop size for the sparse (sNC) and globular (gNC) nanoparticles, where the loop size is defined as the number of beads in the loop.

7 Conclusions

We have performed large-scale simulations of all-polymer nanocomposites, consisting of SCNPs and linear chains. The SCNPs have sparse or globular shape, and half the size of the linear chains. To distinguish the role of the SCNPs in the topological constraints from other specific contributions present in experiments, the simulations for different compositions of the mixture have been performed at constant density, and with identical segmental mobility and monomer excluded volume for the SCNPs and linear chains. Every composition leads to a well-dispersed nanocomposite with fully-penetrated nanofillers. We have investigated the effect of the soft, deformable and penetrable character of the SCNPs on the dynamical properties of the linear matrix. We have found that the introduction of sparse SNCPs, at a 25% in volume fraction, does not alter significantly the dynamics of the linear matrix with respect to the pure linear melt. On the contrary, the globular nanoparticles have a relevant effect already at the volume fraction of 10%, leading to slower dynamics of the linear chains in the nanocomposite than in the pure linear melt.

We have discussed the former observations within the framework of the tube theory. Unlike in systems with hard nanofillers, the SCNPs do not exert geometrical confinement, due to their full penetration by the linear chains. Hence, the SCNPs only contribute to the topological constraints experienced by the linear chains. In order to quantify the strength of the topological constraints,

we have determined the entanglement length N_e of the linear chains, by analysing their isoconfigurational mean paths (IMP) and primitive paths (PP), as a function of the concentration of the SCNPs. In the analysis we have used different estimators proposed in the literature. A clear trend is found for the concentration dependence of the entanglement length in the nanocomposites with globular SCNPs. The analysis of both the IMPs and PPs unambiguously reveals that, within the framework of the tube theory, the linear chains appear to be more entangled in the nanocomposites than in the pure linear melt, with a reduction of up to 30 % of N_e at nanoparticle volume fractions of 60 %.

In the case of the nanocomposites with sparse SCNPs, the value of N_e is essentially unaffected or larger than in the pure linear melt, depending on the used tube representation. Still, the original value for the pure linear chains is just slightly modified by the presence of the sparse SCNPs. This finding is rather different from the neutron spin-echo experimental results on the nanocomposite of Ref.[44] (linear PEO and PMMA-SCNPs), that revealed a noticeable tube dilation with respect to the pure linear PEO. The reasons for such a discrepancy could be among a number of differences between simulated and real systems. For instance, the following ingredients are absent in the simulations (which address the specific role of the SCNP topology) but could make significant contributions to the behavior of the real sample: (i) large dynamic asymmetry characterizing the PEO and PMMA-SCNPs, (ii) relatively high polydispersity (iii), possible changes in the density, that are very difficult to monitor experimentally. Future experiments are planned to determine the actual role of these factors in the dynamics of the nanocomposites.

8 Acknowledgements

We acknowledge financial support from the projects MAT2015-63704-P (MINECO-Spain and FEDER-UE) and IT-654-13 (Basque Government, Spain).

9 Supporting Information

Details of the model and simulation procedure used for generating the nanoparticles. Typical snapshots and additional structural information of the nanoparticles.

References

(1) Kuilla, T.; Bhadra, S.; Yao, D.; Kim, N. H.; Bose, S.; Lee, J. H. Recent advances in graphene based polymer composites. *Prog. Polym. Sci.* **2010**, *35*, 1350 – 1375.

(2) Hussain, F.; Hojjati, M.; Okamoto, M.; Gorga, R. E. Polymer-matrix Nanocomposites, Processing, Manufacturing, and Application: An Overview. *J. Compos. Mater.* **2006**, *40*, 1511–1575.

(3) Baeza, G. P.; Dessi, C.; Costanzo, S.; Zhao, D.; Gong, S.; Alegria, A.; Colby, R. H.; Rubinstein, M.; Vlassopoulos, D.; Kumar, S. K. Network dynamics in nanofilled polymers. *Nat. Commun.* **2016**, *7*, 11368.

(4) Liu, L.; Qi, Z.; Zhu, X. Studies on nylon 6/clay nanocomposites by melt-intercalation process. *J. Appl. Polym. Sci.* **1999**, *71*, 1133–1138.

(5) Kumar, S. K.; Jouault, N.; Benicewicz, B.; Neely, T. Nanocomposites with Polymer Grafted Nanoparticles. *Macromolecules* **2013**, *46*, 3199–3214.

(6) Hashemi, A.; Jouault, N.; Williams, G. A.; Zhao, D.; Cheng, K. J.; Kysar, J. W.; Guan, Z.; Kumar, S. K. Enhanced Glassy State Mechanical Properties of Polymer Nanocomposites via Supramolecular Interactions. *Nano Lett.* **2015**, *15*, 5465–5471.

(7) Pandey, Y. N.; Papakonstantopoulos, G. J.; Doxastakis, M. Polymer/Nanoparticle Interactions: Bridging the Gap. *Macromolecules* **2013**, *46*, 5097–5106.

(8) Hooper, J. B.; Schweizer, K. S.; Desai, T. G.; Koshy, R.; Keblinski, P. Structure, surface

excess and effective interactions in polymer nanocomposite melts and concentrated solutions. *J. Chem. Phys.* **2004**, *121*, 6986–6997.

(9) Ganesan, V.; Jayaraman, A. Theory and simulation studies of effective interactions, phase behavior and morphology in polymer nanocomposites. *Soft Matter* **2014**, *10*, 13–38.

(10) Doi, M.; Edwards, S. F. *The Theory of Polymer Dynamics*; International Series of Monographs on Physics (Book 73); Clarendon Press, 1988.

(11) McLeish, T. C. B. Tube theory of entangled polymer dynamics. *Adv. Phys.* **2002**, *51*, 1379–1527.

(12) Likhtman, A. E.; McLeish, T. C. B. Quantitative Theory for Linear Dynamics of Linear Entangled Polymers. *Macromolecules* **2002**, *35*, 6332–6343.

(13) Bent, J.; Hutchings, L. R.; Richards, R. W.; Gough, T.; Spares, R.; Coates, P. D.; Grillo, I.; Harlen, O. G.; Read, D. J.; Graham, R. S.; Likhtman, A. E.; Groves, D. J.; Nicholson, T. M.; McLeish, T. C. B. Neutron-Mapping Polymer Flow: Scattering, Flow Visualization, and Molecular Theory. *Science* **2003**, *301*, 1691–1695.

(14) Milner, S. T.; McLeish, T. C. B. Parameter-Free Theory for Stress Relaxation in Star Polymer Melts. *Macromolecules* **1997**, *30*, 2159–2166.

(15) Read, D. J.; Auhl, D.; Das, C.; den Doelder, J.; Kapnistos, M.; Vittorias, I.; McLeish, T. C. B. Linking Models of Polymerization and Dynamics to Predict Branched Polymer Structure and Flow. *Science* **2011**, *333*, 1871–1874.

(16) Das, C.; Inkson, N. J.; Read, D. J.; Kelmanson, M. A.; McLeish, T. C. B. Computational linear rheology of general branch-on-branch polymers. *J. Rheol.* **2006**, *50*, 207–234.

(17) Schneider, G. J.; Nusser, K.; Willner, L.; Falus, P.; Richter, D. Dynamics of Entangled Chains in Polymer Nanocomposites. *Macromolecules* **2011**, *44*, 5857–5860.

(18) Li, Y.; Kröger, M.; Liu, W. K. Nanoparticle Effect on the Dynamics of Polymer Chains and Their Entanglement Network. *Phys. Rev. Lett.* **2012**, *109*, 118001.

(19) Pütz, M.; Kremer, K.; Grest, G. S. What is the entanglement length in a polymer melt? *Europhys. Lett.* **2000**, *49*, 735–741.

(20) Likhtman, A. E. Single-Chain Slip-Link Model of Entangled Polymers: Simultaneous Description of Neutron Spin-Echo, Rheology, and Diffusion. *Macromolecules* **2005**, *38*, 6128–6139.

(21) Torquato, S.; Lu, B.; Rubinstein, J. Nearest-neighbor distribution functions in many-body systems. *Phys. Rev. A* **1990**, *41*, 2059–2075.

(22) Chen, Q.; Gong, S.; Moll, J.; Zhao, D.; Kumar, S. K.; Colby, R. H. Mechanical Reinforcement of Polymer Nanocomposites from Percolation of a Nanoparticle Network. *ACS Macro Lett.* **2015**, *4*, 398–402.

(23) Senses, E.; Faraone, A.; Akcora, P. Microscopic Chain Motion in Polymer Nanocomposites with Dynamically Asymmetric Interphases. *Sci. Rep.* **2016**, *6*, 29326.

(24) Mangal, R.; Srivastava, S.; Archer, L. A. Phase stability and dynamics of entangled polymer-nanoparticle composites. *Nat. Commun.* **2015**, *6*, 7198.

(25) Harth, E.; Horn, B. V.; Lee, V. Y.; Germack, D. S.; Gonzales, C. P.; Miller, R. D.; Hawker, C. J. A Facile Approach to Architecturally Defined Nanoparticles via Intramolecular Chain Collapse. *J. Am. Chem. Soc.* **2002**, *124*, 8653–8660.

(26) Gonzalez-Burgos, M.; Latorre-Sanchez, A.; Pomposo, J. A. Advances in single chain technology. *Chem. Soc. Rev.* **2015**, *44*, 6122–6142.

(27) Hanlon, A. M.; Lyon, C. K.; Berda, E. B. What Is Next in Single-Chain Nanoparticles? *Macromolecules* **2016**, *49*, 2–14.

(28) Mavila, S.; Eivgi, O.; Berkovich, I.; Lemcoff, N. G. Intramolecular Cross-Linking Methodologies for the Synthesis of Polymer Nanoparticles. *Chem. Rev.* **2016**, *116*, 878–961.

(29) Altintas, O.; Barner-Kowollik, C. Single-Chain Folding of Synthetic Polymers: A Critical Update. *Macromol. Rapid Commun.* **2016**, *37*, 29–46.

(30) Sun, G.; Guan, Z. Cascade Chain-Walking Polymerization to Generate Large Dendritic Nanoparticles. *Macromolecules* **2010**, *43*, 4829–4832.

(31) Holley, D.; Ruppel, M.; Mays, J.; Urban, V.; Baskaran, D. Polystyrene nanoparticles with tunable interfaces and softness. *Polymer* **2014**, *55*, 58 – 65.

(32) Latorre-Sánchez, A.; Pomposo, J. A. Recent bioinspired applications of single-chain nanoparticles. *Polym. Int.* **2016**, *65*, 855–860.

(33) Pomposo, J. A.; Perez-Baena, I.; Verso, F. L.; Moreno, A. J.; Arbe, A.; Colmenero, J. How Far Are Single-Chain Polymer Nanoparticles in Solution from the Globular State? *ACS Macro Lett.* **2014**, *3*, 767–772.

(34) Perez-Baena, I.; Barroso-Bujans, F.; Gasser, U.; Arbe, A.; Moreno, A. J.; Colmenero, J.; Pomposo, J. A. Endowing Single-Chain Polymer Nanoparticles with Enzyme-Mimetic Activity. *ACS Macro Lett.* **2013**, *2*, 775–779.

(35) Moreno, A. J.; Verso, F. L.; Sanchez-Sanchez, A.; Arbe, A.; Colmenero, J.; Pomposo, J. A. Advantages of Orthogonal Folding of Single Polymer Chains to Soft Nanoparticles. *Macromolecules* **2013**, *46*, 9748–9759.

(36) Lo Verso, F.; Pomposo, J. A.; Colmenero, J.; Moreno, A. J. Multi-orthogonal folding of single polymer chains into soft nanoparticles. *Soft Matter* **2014**, *10*, 4813–4821.

(37) Moreno, A. J.; Lo Verso, F.; Arbe, A.; Pomposo, J. A.; Colmenero, J. Concentrated Solutions of Single-Chain Nanoparticles: A Simple Model for Intrinsically Disordered Proteins under Crowding Conditions. *J. Phys. Chem. Lett.* **2016**, *7*, 838–844.

(38) Lo Verso, F.; Pomposo, J. A.; Colmenero, J.; Moreno, A. J. Simulation guided design of globular single-chain nanoparticles by tuning the solvent quality. *Soft Matter* **2015**, *11*, 1369–1375.

(39) Perez-Baena, I.; Asenjo-Sanz, I.; Arbe, A.; Moreno, A. J.; Verso, F. L.; Colmenero, J.; Pomposo, J. A. Efficient Route to Compact Single-Chain Nanoparticles: Photoactivated Synthesis via Thiol-Yne Coupling Reaction. *Macromolecules* **2014**, *47*, 8270–8280.

(40) Mackay, M. E.; Dao, T. T.; Tuteja, A.; Ho, D. L.; Horn, B. V.; Kim, H.-C.; Hawker, C. J. Nanoscale effects leading to non-Einstein-like decrease in viscosity. *Nat. Mater.* **2003**, *2*, 762 – 766.

(41) Tuteja, A.; Mackay, M. E.; Hawker, C. J.; Horn, B. V. Effect of Ideal, Organic Nanoparticles on the Flow Properties of Linear Polymers: Non-Einstein-like Behavior. *Macromolecules* **2005**, *38*, 8000–8011.

(42) Goldansaz, H.; Goharpey, F.; Afshar-Taromi, F.; Kim, I.; Stadler, F. J.; van Ruymbeke, E.; Karimkhani, V. Anomalous Rheological Behavior of Dendritic Nanoparticle/Linear Polymer Nanocomposites. *Macromolecules* **2015**, *48*, 3368–3375.

(43) Chen, T.; Qian, H.-J.; Zhu, Y.-L.; Lu, Z.-Y. Structure and Dynamics Properties at Interphase Region in the Composite of Polystyrene and Cross-Linked Polystyrene Soft Nanoparticle. *Macromolecules* **2015**, *48*, 2751–2760.

(44) Arbe, A.; Pomposo, J. A.; Asenjo-Sanz, I.; Bhowmik, D.; Ivanova, O.; Kohlbrecher, J.; Colmenero, J. Single Chain Dynamic Structure Factor of Linear Polymers in an All-Polymer Nano-Composite. *Macromolecules* **2016**, *49*, 2354–2364.

(45) Miller, B.; Imel, A. E.; Holley, W.; Baskaran, D.; Mays, J. W.; Dadmun, M. D. The Role of Nanoparticle Rigidity on the Diffusion of Linear Polystyrene in a Polymer Nanocomposite. *Macromolecules* **2015**, *48*, 8369–8375.

(46) Karatrantos, A.; Clarke, N.; Composto, R. J.; Winey, K. I. Entanglements in polymer nanocomposites containing spherical nanoparticles. *Soft Matter* **2016**, *12*, 2567–2574.

(47) Kalathi, J. T.; Kumar, S. K.; Rubinstein, M.; Grest, G. S. Rouse mode analysis of chain relaxation in polymer nanocomposites. *Soft Matter* **2015**, *11*, 4123–4132.

(48) Kalathi, J. T.; Grest, G. S.; Kumar, S. K. Universal Viscosity Behavior of Polymer Nanocomposites. *Phys. Rev. Lett.* **2012**, *109*, 198301.

(49) Riggleman, R. A.; Toepperwein, G.; Papakonstantopoulos, G. J.; Barrat, J.-L.; de Pablo, J. J. Entanglement network in nanoparticle reinforced polymers. *J. Chem. Phys.* **2009**, *130*.

(50) Everaers, R.; Sukumaran, S. K.; Grest, G. S.; Svaneborg, C.; Sivasubramanian, A.; Kremer, K. Rheology and Microscopic Topology of Entangled Polymeric Liquids. *Science* **2004**, *303*, 823–826.

(51) Sukumaran, S. K.; Grest, G. S.; Kremer, K.; Everaers, R. Identifying the primitive path mesh in entangled polymer liquids. *J. Polym. Sci. Part B Polym. Phys.* **2005**, *43*, 917–933.

(52) Kröger, M. Shortest multiple disconnected path for the analysis of entanglements in two- and three-dimensional polymeric systems. *Comput. Phys. Commun.* **2005**, *168*, 209 – 232.

(53) Tzoumanekas, C.; Theodorou, D. N. Topological Analysis of Linear Polymer Melts: A Statistical Approach. *Macromolecules* **2006**, *39*, 4592–4604.

(54) Toepperwein, G. N.; Karayiannis, N. C.; Riggleman, R. A.; Kröger, M.; de Pablo, J. J. Influence of Nanorod Inclusions on Structure and Primitive Path Network of Polymer Nanocomposites at Equilibrium and Under Deformation. *Macromolecules* **2011**, *44*, 1034–1045.

(55) Bisbee, W.; Qin, J.; Milner, S. T. Finding the Tube with Isoconfigurational Averaging. *Macromolecules* **2011**, *44*, 8972–8980.

(56) Kremer, K.; Grest, G. S. Dynamics of entangled linear polymer melts: A molecular-dynamics simulation. *J. Chem. Phys.* **1990**, *92*, 5057–5086.

(57) Bačová, P.; Hawke, L. G. D.; Read, D. J.; Moreno, A. J. Dynamics of Branched Polymers: A Combined Study by Molecular Dynamics Simulations and Tube Theory. *Macromolecules* **2013**, *46*, 4633–4650.

(58) Hoy, R. S.; Foteinopoulou, K.; Kröger, M. Topological analysis of polymeric melts: Chain-length effects and fast-converging estimators for entanglement length. *Phys. Rev. E* **2009**, *80*, 031803.

(59) Hess, B.; Kutzner, C.; van der Spoel, D.; Lindahl, E. GROMACS 4: Algorithms for Highly Efficient, Load-Balanced, and Scalable Molecular Simulation. *J. Chem. Theory Comput.* **2008**, *4*, 435–447.

(60) Rubinstein, M.; Colby, R. H. *Polymer Physics*; Oxford University Press, Oxford, UK, 2003.

(61) Halverson, J. D.; Lee, W. B.; Grest, G. S.; Grosberg, A. Y.; Kremer, K. *J. Chem. Phys.* **2011**, *134*, 204904.

(62) Moreno, A. J.; Colmenero, J. Entangledlike Chain Dynamics in Nonentangled Polymer Blends with Large Dynamic Asymmetry. *Phys. Rev. Lett.* **2008**, *100*, 126001.

(63) Halverson, J. D.; Grest, G. S.; Grosberg, A. Y.; Kremer, K. Rheology of Ring Polymer Melts: From Linear Contaminants to Ring-Linear Blends. *Phys. Rev. Lett.* **2012**, *108*, 038301.

(64) Likhtman, A. E.; Ponmurugan, M. Microscopic Definition of Polymer Entanglements. *Macromolecules* **2014**, *47*, 1470–1481.

(65) Auhl, R.; Everaers, R.; Grest, G. S.; Kremer, K.; Plimpton, S. J. Equilibration of long chain polymer melts in computer simulations. *J. Chem. Phys.* **2003**, *119*, 12718–12728.

(66) Hsu, H.-P.; Kremer, K. Static and dynamic properties of large polymer melts in equilibrium. *J. Chem. Phys.* **2016**, *144*, 154907.

(67) Likhtman, A. E.; Talib, M. S.; Vorselaars, B.; Ramirez, J. Determination of Tube Theory Parameters Using a Simple Grid Model as an Example. *Macromolecules* **2013**, *46*, 1187–1200.

(68) Ge, T.; Panyukov, S.; Rubinstein, M. Self-Similar Conformations and Dynamics in Entangled Melts and Solutions of Nonconcatenated Ring Polymers. *Macromolecules* **2016**, *49*, 708–722.

(69) Tsalikis, D. G.; Mavrantzas, V. G.; Vlassopoulos, D. Analysis of Slow Modes in Ring Polymers: Threading of Rings Controls Long-Time Relaxation. *ACS Macro Lett.* **2016**, *5*, 755–760.

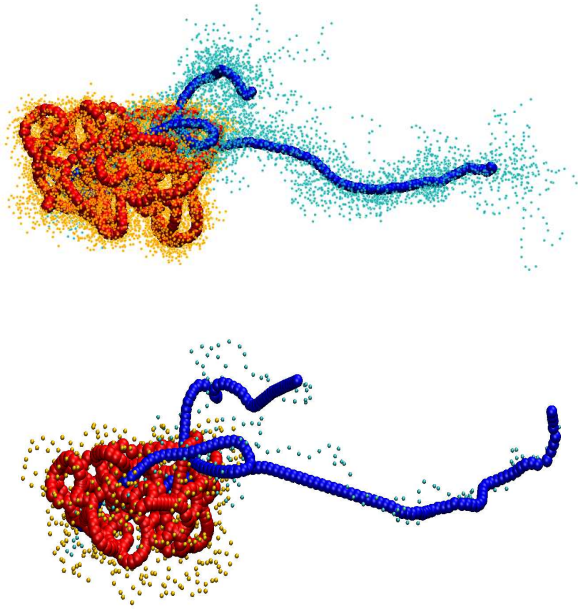

TABLE OF CONTENTS